RSC Advances

ROYAL SOCIETY OF CHEMISTRY

www.rsc.org/advances

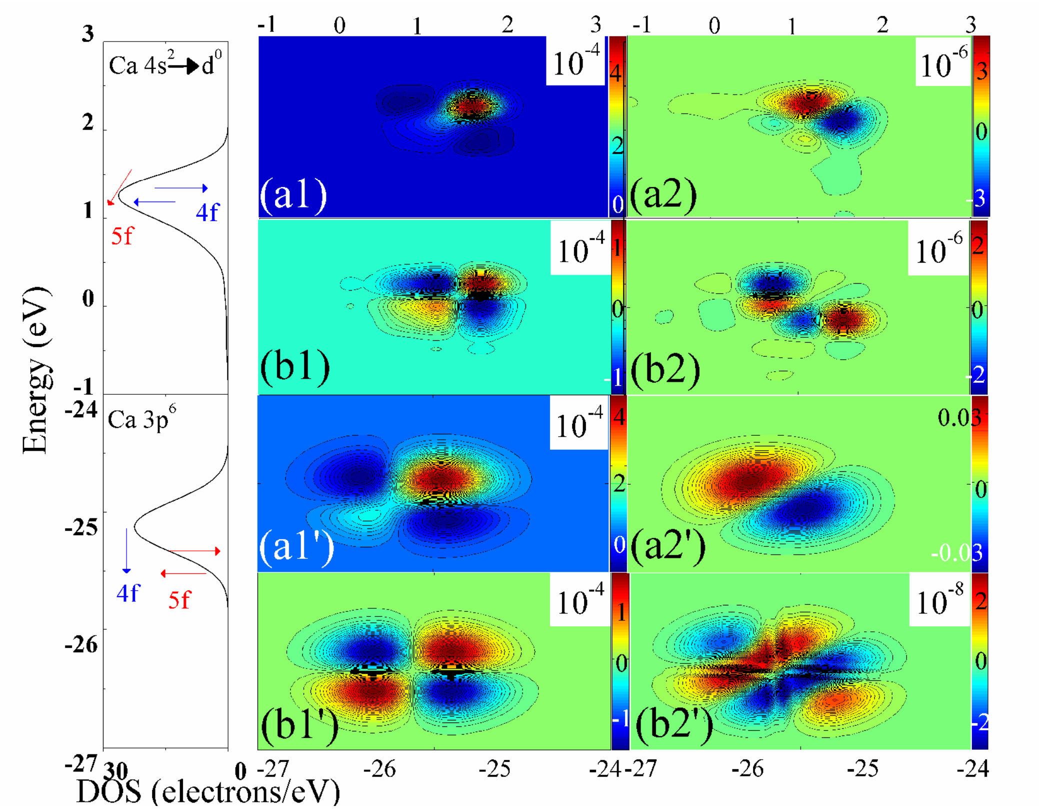

1. The existence states of f-shell electrons in Ca-Mt is calculated via DFT with 2D-CA techniques.

2. Reasons of f-shell electrons influencing on electronic and optical properties are discussed.

3. Electronic and structural phase transitions are systematically analyzed.

DFT and two-dimensional correlation analysis for evaluating the oxygen defect mechanism of low-density 4f (or 5f) elements interacting with Ca-Mt

Liang Bian[1, 2*], Mian-xin Song[2], Fa-qin Dong[2*], Tao Duan[2], Jin-bao Xu[1], Wei-min Li[2], Xiao-yan Zhang[2]

1. Key Laboratory of Functional Materials and Devices under Special Environments, Chinese Academy of Sciences, Urumqi 830011, China

2. Laboratory for Extreme Conditions Matter Properties, South West University of Science and Technology, Mianyang 621010, Sichuan, China

E-mail: bianliang555551@126.com

Tel: +86-0991-3835096; Fax: +86-0991-3835096

Abstract

Understanding how f-shell electrons affect clay minerals is important in an ideal buffer/backfill material. Hitherto, however, there have been few reports that quantitatively simulated the effects of low-density 4f (or 5f) electrons on oxygen defects. Here, we used density functional theory (DFT) and two-dimensional correlation analysis (2D-CA) techniques to calculate the origins of the oxygen defect and electronic transitions of f-shell electrons/Ca type montmorillonite (Ca-Mt) system. We determined the number effect of f-shell electrons to explain the oxygen defects of aluminium-oxygen octahedron and silicon-oxygen tetrahedron at the valence band, which is consistent with the orbital fluctuation results. This study offers a new method for explaining the oxygen defect mechanism.

Keywords: f-shell electrons, montmorillonite, two-dimensional correlation analysis, density functional theory

1. Introductions

Extensive information has been collected on the effects of radiation on clay minerals, namely, montmorillonite, kaolinite, and illite, providing a wealth of information on environmental and geological processes [1-2]. The applications include the reconstruction of past radioelement migrations and evolution of the physical-chemical properties [3, 4]. Several clay minerals have been studied, by electron paramagnetic resonance spectroscopy, on the defects produced by natural or artificial radiation [5, 6]. These defects mostly consist of electron holes located on the oxygen atoms of the structure. Most radiation-induced defects are associated with a π orbital on a Si–O bond. The most abundant defect in clay minerals is oriented perpendicular to the silicate layer [7-9]. As part of investigations of the inner cation exchange in buffer materials, previous experiments have reported the ion exchange and surface-mediated reduction mechanisms. For example, Bradbury et al [10-11] quantified the influence of competition between metals (Co, Ni, Zn, Eu, Nd, Am, Th and U) in different valence states on their individual sorption characteristics under conditions dominated by pH-dependent sorption on Na^- and Ca-Mts. The competition between divalent transition metals and trivalent lanthanides indicated that multiple sets of strong sites exist as subsets of the 40 $mmol\cdot kg^{-1}$ of weak sites present in the Mt conceptual model. Differences in sorption behaviour are indicative of the surface-mediated transformation of atomic charge that has been reported for a number of redox-active and redox-inactive minerals [12].

Currently, there has been growing interest in studying the adsorbing property of Mt from a molecular point of view [13]. In 2010, Martorell et al [14] used density functional theory (DFT) to calculate the adsorption of uranyl on bare and solvated models of the octahedral (001) surface of Mt, and the authors determined the relative stable adsorbing property on the AlO-Al (H) bridges. The uranyl at the AlOO(H) short-bridge site exhibits a f-p interaction due to the electrons transfer from uranyl to the nearest oxygen atoms, which is in agreement with the results of Glezakou [15]. In 2012, Suter et al [16] studied the molecular mechanism of surface complexation and diffusivity of Cs in Mts with the Grand Canonical Monte Carlo (GCMC) simulation. The octahedral layer composition and possible role of the interlayer cations reflect that the migration of the proton across the octahedral vacancy takes place by means of a stable intermediate in which the proton is coordinated with an apical oxygen, and a Si-O basal bond is broken so that the Si coordinates with the O that releases the H, stabilising its residual charge [17, 18]. These reports enabled us to develop a new idea for investigating the electronic transition of Mt [19].

Theoretically, knowledge on electron and hole transfer is important for deep oxygen defects of f-shell electrons adsorbing in montmorillonite. For example, Pieterson et al [20] reported on the intera configurational $f^{n}\rightarrow f^{n-1}d$ transitions. The lack of research is partly from the fact that the transitions generally lie in the vacuum regions. Additionally, the 5d orbital is much more extended than the 4f, and most of the intensity is in vibronic bands. The Coulomb interaction and spin-orbit coupling parameters for the $4f^{n-1}$ core are related to the f-d Coulomb interaction using Cowan’s code [21]. Between 2012 and 2013, Dorenbos [22, 23] calculated the chemical model and absolute binding energy of 4f-shell electrons in lanthanide doping. The 4f-electron binding energy depends on the charge of the lanthanide ion and its environment, where the n numbers of [Xe] $4f^n$ correspond to the trivalent (n), tetravalent (n-1) and divalent (n+1), respectively. Additionally, the binding is strong when the $4f^n$ shell is halfly (n=7) or completely filled (n=14) and it is relatively weak when there are one or eight electrons in the 4f-shell electrons. Therein, the Coulomb repulsion between a 4f-shell electron and anion is shifted towards weaker bonding with respect to the binding energy (4f-HRBE), and the author provided the 4f-electron binding energy relative to the vacuum energy (4f-VRBE). For the hybridisation between 5f-shell electron's orbital and O-$2p^4$ orbital, Hasegawa et al [24] investigated the f-p model, which is the more realistic Hamiltonian for the 5f-shell electron influencing the O-$2p^4$ orbitals, to better understand the electronic structure of 5f-O-p. There has been a peculiar point in which the octupole phase only appears for the small absolute value of (f-p π) / (f-p σ), where (f-p π) and (f-p σ) are the Slater-Koster integrals between f and p orbitals [25]. The cause of the sensitivity of the octupole ordered phase for the f-p interaction is not yet well understood. It is useful to extract the oxygen defects in silicon-oxygen tetrahedron and octahedral aluminium oxide.

Currently, the electronic transitions of low-density 4f (or 5f) elements interacting with Ca-Mt remain unclear. In the experiment [26], the 4f lanthanides reduce the oxygen vacancy formation energies and the small narrowing of energy gap has been attributed to the defect states of oxygen vacancy. Usually, the surface of Mt becomes charged and it has to be compensated by the adsorption of certain ions [27, 28]. The charge compensation creates an oxygen vacancy defect on the O-2p^4 electronic structures, and the defect sites are near-randomly distributed [29]. To date, simulations have rarely been used in research into the origin of low-density 4f (or 5f) elements and Ca-Mt for understanding the possible oxygen defects. The purpose of this paper is to quantify the effect of f-shell electrons of low-density 4f (or 5f) elements incorporated into Ca-Mt to improve our understanding of the stability issues. Here, we calculate the orbital fluctuations of f-shell electron/Ca-Mt via a new static technique, the DFT with two-dimensional correlation analysis (2D-CA) method, which has been successfully used in Fourier transform infrared spectroscopy, 2D correlation dielectric relaxation spectroscopy and nuclear magnetic resonance spectroscopy [30-32]. The effect of accumulated f-shell electrons was calculated, where the final orbital fluctuations were analyzed from the all PDOS results of f^n-shell electrons (n=1~14). The possible origins of the static electron transfer processes are discussed. Therein, the electronic structures were obtained from the results of all optimized models.

2. Computational details

In this work, the Ca-Mt in the space group C2/m included two Ca ions and dioctahedral 2:1 phyllosilicates, which have one octahedral sheet sandwiched between two tetrahedral sheets [33, 34]. The tetrahedral sheets are formed by linking tetrahedral oxygen atoms through three shared basal oxygen atoms in each tetrahedron. Hydroxyl groups, together with the free unlinked fourth apical oxygen atom, form the tetrahedral to the octahedral sheets. The most common ion occupying the octahedral site is Al^{3+}, and the most common ions occupying the tetrahedron are

Si^{4+} and Al^{3+}. In the dioctahedral 2:1 phyllosilicates, only two-thirds of the octahedron is occupied. If the vacancies are cis with respect to the hydroxyl groups, the phyllosilicate is designated cis-vacant; otherwise, it is trans-vacant. In our studies, we focus on the trans-isomer, which is more prevalent in nature. Therein, Fig. 1 a) shows that the Ca1 atom is close with respect to the 4f (or 5f) element, and the bond length is 0.62 nm. Additionally, the Ca2-O bond length is 0.32 nm.

In the Ca-Mt interlayer, the free volumes describe the all possible adsorbing sites of 4f (or 5f) element [35]. The probability of insertion for probes into Ca-Mt was changed with the cell of 4f (or 5f) elements and Ca-Mt [36, 37]. The initial free volume (0.199 nm^3) is illustrated in the interlayer region (Fig. 1 a)). We determined the average adsorption sites and capacities of 4f (or 5f) elements, over a wide range of temperatures (298~698 K), using a 10,000,000-step Grand Canonical Monte Carlo (GCMC) simulation via the Metropolis methods (Sorption, Materials studio, Accelrys, USA). The 4f (or 5f) elements were lanthanide atoms from lanthanum to lutetium (or actinide atoms from actinium to lawrencium). As shown in Fig. 1 b), the adsorption process is corroborated by the short-range van der Waals energy between the 4f (or 5f) elements and surface O. Temperature control was achieved using an Andersen caldarium, and the equation of motion was integrated using the Verlet algorithm. When the layer charge and potential of the system reach equilibrium, there are some 4f (or 5f) elements close to the Ca atoms in the interlayer of Ca-Mt [38]. The 4f (or 5f) elements occupy the partial free volumes (0.199 $nm^3 \rightarrow$5f: 0.121~0.132 nm^3; and 4f: 0.117~0.131 nm^3). The max adsorption capacities are 252.0~291.0 $mg \cdot g^{-1}$ (5f) and 154.2~194.2 mg·g^{-1} (4f), respectively, which is consistent with the experimental results [39-40].

The final structural was relaxed by 200 ps molecular dynamics (MD) with isothermal-isobaric (NPT)-isothermal-isochoric (NVT) ensembles (Discover module in the Materials Studio) [41]. The short range van der Waals term was calculated using the atom based method. The Ewald+Group summation method for the long-range electrostatic interaction term was routinely used to evaluate the electrostatic interactions in reasonably small models [42]. The interatomic potentials for the Ca-Mt to 4f (or 5f) elements were obtained from the parameterised universal force field (UFF) method [43]. The f-p and f-d hybrid orbitals escalate the activation energies (E) within 0.64~2.25 eV, showing an expanded interlayer, as illustrated in Fig. 2. The 4f (or 5f) elements occupy the neighbouring Ca atomic diffusion paths, enlarging the layer distances from 0.48 nm to 0.48~0.50 nm. The low potential energy Ca (~-0.02 eV) atom is tightly bound to the surface O (~-0.01 eV) atom, whereas the improved surface potentials of Ca-4s^2-O-2p^4 hybrid orbitals induce Ca and O atoms to close to each other (Ca-O bond length: 0.62 nm→0.43 nm). The relative diffusion coefficient decreases (7.8 ×10^{-9} m^2·s^{-1}→5f: 1.1~4.4 ×10^{-9} m^2·s^{-1}; 4f: 1.1~2.4 ×10^{-9} m^2·s^{-1}), as shown in Table 1. In this case, the 5f^n orbital splits at the conduction band (Ca-4s^2) and valence band (O-2p^4), providing more quantum wells than that of 4f^n orbital for restricting the perpendicular cationic diffusion. For the interlayers, the oxygen defect enhances the O-O long-range orbital degeneracy to narrow the angle, changing the O-Si-O and O-Al-O bond angles as follows: 140°→124~142° and 78~79°→56~70°, respectively. The relative torsional degree ((angle difference)/initial angle) of the Al-O angle (11.9~29.1%) is higher than that of the Si-O angle (1.4~11.4%); therefore, the inner structural damage is attributed to the aluminium-oxygen octahedron (0.168~0.176 nm→0.163~0.173 nm), correlating with the electronic structure results.

After determining the adsorption structures, we calculated the imaginary part of the dielectric functions (ε) and Mulliken charges using the Kramers-Kronig transformation (Castep module in the Materials Studio) [44, 45]. Pseudo atomic calculations are performed for Ca-$2p^6 3s^2 3p^6 4s^2$, Al-$3s^2 3p^1$, Si-$3s^2 3p^2$, O-$2s^2 2p^4$, $5f^{0\sim14} 6d^{0\sim2} s^2$ and $4f^{0\sim14} 5d^{0\sim1} s^2$. Low frequency is related to the weak electronic interaction, such as the long-range electrostatic potential of the Ca-Ca bonds. Ultimately, we found that the orbitals of f-shell electrons simultaneously hybridize with the Ca and O orbitals on the long-range surface layer and short-range inner layer, due to the similar crystalline electric field (CEF) potential energy, where the hopping integrals (f-p π and f-p σ terms) in the f-p hybridization term of Hamiltonian formula by using Slater-Koster table provide the similar hopping amplitudes between f and p orbitals [24]. In this context, the electron transfer rates of the major constituents have the following order: Si-$3p^2$ ~ Al-$3p^1$ << Ca-$4s^2 \rightarrow d^0$ < Ca-$3p^6$ < O-$2p^4$. On the other hand, compared to that of 4f-shell electrons/Ca-Mt, the orbital degeneracy of 5f-shell electrons/Ca-Mt reduces near the Fermi point, accelerating the electron transfer process at the conduction band and valence band. The electronic transition intensities have the following order: $E_{4f\text{-}Al} < E_{5f\text{-}Al} < E_{4f\text{-}Si} < E_{5f\text{-}Si} < E_{4f\text{-}Ca} < E_{5f\text{-}Ca} < E_{4f\text{-}O} < E_{5f\text{-}O}$. This theoretical oxygen defect mechanism is consistent with the experimental results

[35-41]. Notably, the surface Ca and O atoms preferentially provide the active p (and empty d) orbitals to hybridize with the orbitals of f-shell electrons. The strong interactions in the 5f (or 4f)-Ca f-partial (d–p) π-bond orbital weaken the 5f (or 4f)-Ca potentials at -1.4 eV [46] when the electron transfer rates of O-$2p^4 \rightarrow$Ca-d^0 are reduced. The electronic transition results will be discussed with the hybrid orbital simulations.

To better understand the electron transfer processes, we calculated the partial density of states (PDOS) via non-dispersion corrected DFT. For the exchange-correlation functional, the generalised gradient approximation (GGA) was used, especially Perdew-Burke-Ernzerhof (PBE) parametrisation [47] (Castep module in the Materials Studio). This method has been demonstrated to rather accurately describe adsorption systems [48]. Therein, Ca $3p^6 4s^2$ electrons interact with the f electrons, and then there is a f-p interaction at the top of the valence band of O $2p^4$ electrons [49]. Ultrasoft pseudo potentials are used [50], and the SCF tolerance is 2×10^{-6} eV·atom^{-1}. A gamma-centred 2×2×1 Monkhorst-Pack k-point grid was used to sample the Brillouin zone, while the calculations were restricted to the Γ point because of the large size of the unit cell. This technique has little computational overhead compared to the DFT-D2 and vdW-TS methods (Table 2). High f-shell electronic potentials strengthen the Si-O and Al-O interaction based on comparisons with the initial data. The calculated accuracy is close to the experimental and theoretical results [7-15].

Because the orbital contribution of a low concentration of 4f (or 5f) electrons can not be calculated based on the increase in the number of the f-shell electrons, the virtual crystal approximation (VCA) method underestimates the electron exchange interactions [51]. For this purpose, we used a quantitative two-dimensional correlation analysis (2D-CA) technique to better understand the orbital fluctuation of f-shell electron/Ca-Mt (Matlab, MathWorks, USA) [52, 53] (Eqs. (1) and (2)). This method resolves the problem of quantitative analysis of the orbital degeneracy of low concentrations of 4f (and 5f) electrons and reflects the electron transfer process of the electron wave function. As shown in Fig. 3, the orbital fluctuation intensity and range reflect the electronic transition of f-shell electrons/Ca-Mt according to the synchronous and asynchronous data [54]. The statistic electron transfer process can be studied through calculations of the synchronous ($\Psi_{(e1,\ e2)}$) and asynchronous ($\Phi_{(e1,\ e2)}$) patterns. The PDOS is formally defined as the dynamic spectrum $\tilde{y}_{(e,\ c)}$ of a system associated with the application of an external perturbation. If $\Psi_{(e1,\ e2)}\times\Phi_{(e1,\ e2)}>0$, the PDOS intensity variation observed for e1 predominantly occurs before that observed for e2, implying that there is enhancement of the localised hybrid orbital. This enhancement of the localised hybrid orbital can reflect the effect of f-shell electron accumulation on the outer electron orbitals. For example, the accumulated f-shell electron orbitals degenerate to the localised O-2p^4 orbital near the Fermi point. With the increase in the number effect of f-shell electrons, the f-p degeneracy is enhanced, showing the appearance of more active electrons at the O-2p^4 orbital, which is consistent with the result of effective electron masses.

$$\Psi_{(e1,e2)} = \frac{1}{m-1}\sum_{j=1}^{m} \tilde{y}_{j(e1)} \cdot \tilde{z}_{j(e2)} \ . \qquad (1)$$

$$\Phi_{(e1,e2)} = \frac{1}{m-1}\sum_{j=1}^{m} \tilde{y}_{j(e1)} \cdot \tilde{y}_{j(e2)} \qquad j = 1,2,\ldots,m \qquad (2)$$

where $\Psi_{(e1,\ e2)}$ is regarded as a measure of the dissimilarity in the PDOS intensity variations. $z^{\sim}_{j(e2)}$ can be directly obtained from PDOS as the dynamic spectra $y^{\sim}_{j(e1)}$ by applying a simple linear transformation operation and Hilbert-Noda transformation matrix method [55]. $\Phi_{(e1,\ e2)}$ represents the overall similarity or coincidental tendency between two separate intensity variations measured between different PDOS variables.

3. Results and discussion

3.1. Partial density of the states of f-shell electrons/Ca-Mt.

The effects of the f-shell electron on the orbital fluctuation are chiefly ascribed to near-degenerate orbitals as a function of the cumulative electron events in f-shell electrons, Ca-Mt. The Kohn-Sham electron band structure was evaluated while considering a specific path inside the Brillouin zone, which is included in the supporting information; the high symmetry points are also depicted. The full band structure is shown at the top of Fig. 4, and there is a set of three deep bands between 0.8 and 0.95 eV. Above them, the top valence bands (VB) are mainly filled with Ca^{2+}-$4s^2$ electrons in characters, but there is a significant contribution from the O-$2p^4$ states. The bottom of the conduction band (CB) is also originated from the O-$2p^4$ and Ca-$4s^2$ orbitals, but the O-$2p^4$ contribution is relevant for energies above 0.5 eV. At the bottom part, there is a close-up of the band structure near the Kohn-Sham band gap, where we can see the valence band maximum and conduction band minimum at the G point. Qualitatively, the direct gaps are 0.8 eV and the secondary indirect gap displays slightly larger energies, which are as follows: 0.95 eV between the G point at the valence band and Q point at the conduction band. The PDOS curves for f-shell electrons/Ca-Mt reveal the change in the electron transfer process near the Fermi point. These peak structures are due to the electronic transitions between the O-2p uppermost valence bands and the 5d (or 6d) conduction bands just above the main band gap. The number of the f-shell electrons is a variable factor. They fill the particle energy levels of the empty d orbital at the conduction band. When the f-shell electrons reach the half-filled state (n=7), the degeneracy of the f and d orbitals causes weak d-f hybridisation [56], enhancing the electron transfer rate of Ca-4s^2. At the valence band, the Al-3p^1, Si-3p^2 and Ca-3p^6 potentials reduce with the degeneracy-split localised energy levels at -15.5, -6 and -25.7 eV, respectively, with the increase in the number of the f-shell electrons.

It should be noted that the sharp PDOS peaks of the top of the valence band and the bottom of the conduction band are related to the localisation of the wave functions, corresponding to the highest occupied (Ca-4s^2) and lowest (O-2p^4) unoccupied orbitals. At the top of the valence band, one can see that there is a strong f-O-2p^4 hybrid interaction, showing the enhanced PDOS intensity of O-2p^4 orbital [14]. It is a contribution of f-p σ hybrid orbital for the oxygen vacancy defect. In contrast, the bottom of the conduction band is dominated by the Ca-4s^2 orbital. A part Ca-4s^2 orbital fill in the low-energy d orbital near the Fermi point, due to the orbital of f-shell electron degenerates to Ca-4s^2 orbital [57]. Therefore, it creates a long-range f-Ca-O-(Si) d-p π hybrid orbital.

3.2. f-Ca orbital hybridisation at the conduction band.

To fully and quantitatively understand the electronic transitions, we calculated the dielectric functions and surface potentials, as indicated in Fig. 5. Crystal field theory indicates that the f bands split into two $f^{5/2}$ and $f^{7/2}$ states with angular momenta of j=5/2 and j=7/2, respectively, because of the spin-orbit coupling. Only the $f^{7/2}$ state is fully occupied with the six f electrons. It degenerates to neighbouring Ca-$3p^6$ orbitals, creating a new f-Ca f-p σ hybrid orbital. Crystal field splits the $f^{5/2}$ state into two independent time-reversal invariant momentum points at the G point. Some of the $f^{5/2}$ electrons jump into the empty 5d (or 6d) orbitals, splitting into two-fold degeneracy (e_g) and triple degeneracy (t_{2g}) states. Such an enhanced d orbital can easily hybridize with a Ca-$4s^2$, resulting in the formation of a new f-Ca s-d π hybrid orbital. Therefore, the interlayer $f^{5/2}$ electrons cut off the initial Ca-Ca p-p σ orbital. With the increase in the number of the f-shell electrons, the highly sensitive f-d π hybrid orbital weakens the p-p σ bond strength of the long-range Ca-Ca bond.

Normally, changing the composition of a mixture consisting of strongly interacting species will result in a position shift of some of the component bands. The contributions of the $d^{0\sim1}$ orbital and weak f-d hybridisation were ignored due to the stable degenerate s-d orbital and low concentration. The number of f-shell electrons was the only factor for the change in the orbital fluctuation. As shown in Fig. 6, we obtained the numerical energy gradients of the long-range f-Ca orbitals. The full-filled $f^{7/2}$ state just transfers the f-Ca f-p σ hybrid electron into a low-energy orbital (-25 eV→-26 eV). For the Ca s-d^0 π model, the half-filled $f^{5/2}$ states cause the Ca-$4s^2$

electrons to jump into the low-energy d_z orbital from 1.5 eV to 0.9 eV. This strengthens the degeneracy of the energy levels of oxygen at -2.5 eV. There is a different electron transfer process for the 4f-shell and 5f-shell systems. The $5f^{5/2}$ state shows that the band position shift is coupled with a simultaneous intensity increase. It provides an accumulation of the energy levels at the conduction band, producing many additional effective holes (41.86~43.04 10^{-31} kg); see Table 3. The $4f^{5/2}$ state shows the electron orbital variations arising from the classical intensity changes of two highly overlapped bands with a fixed band position and relative line shape. One band (1.5 eV) decreases in intensity quickly, while the other band (1 eV) increases in intensity much more gradually, as indicated by the two arrows.

Furthermore, the surface charge transition with $Ca^{2+} \rightarrow Ca^{+}$ is a key factor for the electronic transitions in the Ca-Mt system. This is owing to the fact that the f-d hybrid orbital provides many energy levels at the conduction band, releasing additional effective electrons to annihilate particle cationic holes. The empty d orbital can hybridize with some $f^{5/2}$ orbital at the bottom of the conduction band due to the charge compensation. Therefore, the Mulliken charges (0.47~0.49 e) of Ca^{2+} are clearly reduced, even 0.14~0.2 e (mono-valent Ca^{+}) for the effect of $5f^{n}$-shell electrons (n<7), as shown in Table 4. Notably, the unstable $f^{5/2}$ state of $5f^{n}$-shell (n<7) electrons causes the $6d_{z2}$ orbital to degenerate to the partial Ca-$4s^2$ orbital. This process creates an empty Ca-d^0 orbital to produce one new high-energy f-d^0 hybrid orbital. The O-Ca electron transfer process changes from O-$2p^4 \rightarrow$Ca-$3p^6$ to O-$2p^4 \rightarrow$empty Ca-d^0. This charge transition phenomenon has been characterised by cation exchange experiments, such as Eu [58], Am, Th, Np and U [8, 9].

3.3. Oxygen defects of silicon-oxygen tetrahedron and aluminium-oxygen octahedron at the valence band.

In the opinion of Tsipis et al [59], the electron ionisation effects attributable to the f-shell electrons vary as a function of the cumulative number of electron events. The additional loss produces gap defects (V), vacancy type defects (V_n) and a vacancy colour centre (V_c) at cation energy levels, which can easily form V-O interstitial (Oi), V_n-O_i and V_c-O binding. With the loss of O valence electrons, the new V_c provides a secondary strong electronic energy to transfer O-$2p^4$ electrons (whose low affinity energy is 141 kJ·mol^{-1}) [60]. However, the adsorption model of low-density 4f (or 5f) elements in Ca-Mt, ignoring the irradiation in this work, is mainly decided by the van der Waals energy between the 4f (or 5f) elements and Ca-Mt. Fig. 7 explains the quantitative electronic transition of oxygen atoms in the silicon-oxygen tetrahedral and aluminium-oxygen octahedral layers. The $5f^{5/2}$ state seriously splits the O-$2p^4$ energy level (-2.5 eV) into a pair of high-energy and low-energy bands, which reflects that the integral intensity of the O-$2p^4$ energy level peak is kept at a constant value; therefore, the peak height decreases gradually as the band width is increased. Additionally, the crystal field splits the $4f^{5/2}$ state into three low energy levels near -2.5 eV. Therefore, the $f^{5/2}$ state chiefly hybridizes with the O-p_y orbital that the orbital fluctuation creates two 2p-hole defects (O_i) in the valence band region (near the -2.5 eV potential fields). The delocalised O atomic charges decrease from -0.31~-0.24 e to -0.31~-0.15 e (5f) and -0.3~-0.18 e (4f).

As a general rule, the V_c defect is occupied by the increased f carriers; then, it jumps into the high-energy orbital of localised cations. Considering the electron loss being compensated, we calculated the quantitative electron transfer processes, as shown in Fig. 8. For the aluminium-oxygen octahedral structure, a 2p-hole defect weakens the density of the sp3d2 hybrid orbitals of covalent Al-O $3p^1$-$2p^4$ orbitals, which creates a new peak of energy levels from an Al-$3p^1$ orbital transferring into similar energy levels of two Al-$3s^2$ orbitals to become an Al-O s-p π-bond orbital. The new π electron orbital variations arise from the classical intensity changes of two highly overlapped bands with a fixed band position and relative line shape (-16~-15 eV), such as the shape for Ca-$4s^2$→d. While the Al-O bonds are relatively stable due to the low probability of Al-$3s^2$ orbital occupation, this can usually be characterised by experiments [16].

Although the silicon-oxygen tetrahedron is effective for maintaining the stable Mulliken charges of Si (0.51 e) atoms, the weak surface O-$2p^4$ electronic density decreases the short-range Si-O p-p orbital degeneracy. Therein, one Si-O sp3 hybrid orbital and four oxygen p orbitals in the tetrahedron form four σ bonds with 50% ionic bond and 50% covalent bond character in the ground state phase. Additionally, the empty Si-3d orbital can act as a key by a d-orbital participation that forms two unstable hybrid orbitals, p-d π of sp3d. Hence, the Si-O bond lengths increase (0.141~0.159 nm→0.152~0.158 nm) with the total surface potential strengthening (-0.02 eV→-0.015 eV). This is a secondary factor for the oxygen defect in the f-Ca-Mt system.

4. Conclusions and Summary

In summary, we discussed the oxygen defects and electronic transitions of f-shell electron/Ca-Mt models, using the DFT and 2D-CA techniques. We briefly discussed the number of the f-shell electrons affecting the orbital fluctuation and electron defects of the aluminium-oxygen octahedron and silicon-oxygen tetrahedron. The accumulated valence electrons at the O-$2p^4$ energy levels create a vacancy colour centre (V_c), providing many effective electrons. The enhanced Al-O sp3d2 and Si-O sp3 hybrid orbitals induce the Si-O and Al-O bond lengths to be shortened. As a result, it can be used to explain the proposed oxygen defect mechanism. In addition, the origin of the Ca^{2+}-Ca^{+} charge transition was discussed due to the f-Ca orbital hybridisation at the conduction band.

We discussed the analysis of the influence of the number of the f-shell electrons on the electronic transitions of Ca-Mt. However, these results are insufficient for calculating the f-shell dynamical radiation processes to better understand the crystal phase transitions and atomic decay in ageing processes. This work, however, provides useful information on how to determine the quantitative electronic transition of the f-Mt system. This study introduces a new perspective to the design and development of a high-stability Ca-Mt-based buffer layer.

Acknowledgments

The authors acknowledge the financial supports by National Natural Science Foundation of China (41302029, 41130746, 41272050 and 41302027), International Technology Cooperation Foundation of Autonomous Region (20136009), West Light Foundation of The Chinese Academy of Sciences (RCPY201206), Key Fund Project of Sichuan Provincial (13ZA0163 and 2012JYZ002), Science and Technology Program of Urumqi (Y131020006) and Fundamental Science on Nuclear Waste and Environmental Security Laboratory (12zxnp05).

References

[1] A. Meleshyn, M. Azeroual, T. Reeck, G. Houben, B. Riebe, C. Bunnenberg, Influence of (Calcium−)Uranyl−Carbonate Complexation on U(VI) Sorption on Ca- and Na-Bentonites, Environmental Science & Technology, 2009, 43, 4896–4901

[2] T. H. Wang, T. Y. Liu, D. C. Wu, M. H. Li, J. R. Chen, S. P. Teng, Performance of phosphoric acid activated montmorillonite as buffer materials for radioactive waste repository, Journal of Hazardous Materials, 2010, 173, 335-342

[3] M. Ikeda, T. Yoshii, T. Matsui, T. Tanida, H. Komatsu, I. Hamachi, Montmorillonite-Supramolecular Hydrogel Hybrid for Fluorocolorimetric Sensing of Polyamines, Journal of the American Chemical Society, 2011, 133, 1670-1673

[4] T. Allard, E. Balan, G. Calas, C. Fourdrin, E. Morichon, S. Sorieul, Radiation-induced defects in clay minerals: A review, Nuclear Instruments and Methods in Physics Research Section B: Beam Interactions with Materials and Atoms, 2012, 277, 112-120

[5] P.L. Hall, The application of electron spin resonance spectroscopy to studies of clay minerals: I. Isomorphous substitutions and external surface properties, Clay Minerals, 1980, 15, 321-335

[6] M. Plötze, , G. Kahr, R. Hermanns Stengele, Alteration of clay minerals-gamma-irradiation effects on physicochemical properties, Applied Clay Science, 2003, 23, 195-202

[7] T. Allard, G. Calas, Radiation effects on clay mineral properties, Applied Clay Science, 2009, 43, 2, 143-149

[8] C. Fourdrin, T. Allard, I. Monnet, N. Menguy, M. Benedetti, G. Calas, Effect of Radiation-Induced Amorphization on Smectite Dissolution, Environmental Science & Technology, 2010, 44, 2509-2514

[9] S. Chakraborty, F. Favre, D. Banerjee, A. C. Scheinost, M. Mullet, J. J. Ehrhardt, J. Brendle, L. Vidal, L. Charlet, U(VI) Sorption and Reduction by Fe(II) Sorbed on Montmorillonite, Environmental Science & Technology, 2010, 44, 3779-3785

[10] M.H. Bradbury, B. Baeyens, Experimental measurements and modeling of sorption competition on montmorillonite, Geochimica et Cosmochimica Acta, 2005, 69, 4187-4197

[11] M.H. Bradbury, B. Baeyens, Modelling the sorption of Mn(II), Co(II), Ni(II), Zn(II), Cd(II), Eu(III), Am(III), Sn(IV), Th(IV), Np(V) and U(VI) on montmorillonite: Linear free energy relationships and estimates of surface binding constants for some selected heavy metals and actinides, Geochimica et Cosmochimica Acta, 2005, 69, 875-892

[12] J. Shi, H. Liu, Z. Lou, Y. Zhang, Y. Meng, Q. Zeng, M. Yang, Effect of interlayer counterions on the structures of dry montmorillonites with Si^{4+}/Al^{3+} substitution, Computational Materials Science, 2013, 69, 95-99

[13] F. Q. Zhang, W. Guan, Y. T. Zhang, M. T. Xu, J. Li, Z. M. Su, On the Origin of the Inverted Stability Order of the Reverse-Keggin $[(MnO_4)(CH_3)_{12}Sb_{12}O_{24}]^{6-}$: A DFT Study of α, β, γ, δ, and ε Isomers, Inorganic Chemistry, 2010, 49, 5472-5481

[14] B. Martorell, A. Kremleva, S. Krüger, N. Rösch, Density Functional Model Study of Uranyl Adsorption on the Solvated (001) Surface of Kaolinite, Journal of Physical Chemistry C, 2010, 114, 13287-13294

[15] V.A. Glezakou, W.A. deJong, Cluster-Models for Uranyl(VI) Adsorption on α-Alumina,

Journal of Physical Chemistry A, 2011, 115, 1257-1263

[16] J.L. Suter, M. Sprik, E.S. Boek, Free energies of absorption of alkali ions onto beidellite and montmorillonite surfaces from constrained molecular dynamics simulations, Geochimica et Cosmochimica Acta, 2012, 91, 109-119

[17] S.V. Churakov, Mobility of Na and Cs on Montmorillonite Surface under Partially Saturated Conditions, Environmental Science & Technology, 2013, 47, 9816–9823

[18] D.M. Santiburcio, M. Kosa, A.H. Laguna, C.I. Sainz-Díaz, M. Parrinello, Ab Initio Molecular Dynamics Study of the Dehydroxylation Reaction in a Smectite Model, Journal of Physical Chemistry C, 2012, 116, 12203-12211

[19] S. H. Yeon, J. Seol, Y. J. Seo, Y. Park, D. Y. Koh, K. P. Park, D. G. Huh, J. Lee, H. Lee, Effect of Interlayer Ions on Methane Hydrate Formation in Clay Sediments, Journal of Physical Chemistry B, 2009, 113, 1245-1248

[20] L. Pieterson, M. F. Reid, R. T. Wegh, S. Soverna, A. Meijerink, $4f^n \rightarrow 4f^{n-1}5d$ transitions of the light lanthanides: experiment and theory, Physical Review B, 2002, 65, 045113-045129

[21] R.D. Cowan, The theory of atomic structure and spectra, University of California press, Berkeley, 1981

[22] P. Dorenbos, Modeling the chemical shift of lanthanide 4f electron binding energies, Physical Review B, 2012, 85, 165107-165116

[23] P. Dorenbos, Determining binding energies of valence-band electrons in insulators and semiconductors via lanthanide spectroscopy, Physical Review B, 2013, 87, 035118-035125

[24] Y. Hasegawa, T. Maehira, T. Hotta, Key role of hybridization between actinide 5f and oxygen 2p orbitals for electronic structure of actinide dioxides, Condensed Matterals, 2013, 12, 1-8

[25] K. Kubo, T. Hotta, Analysis of fp model for octupole ordering in NpO_2, Physical Review B, 2005, 72, 132411-132415

[26] S.W. Chen, J.M. Lee, K.T. Lu, C.W. Pao, J.F. Lee, T.S. Chan, J.M. Chen, Bandgap narrowing of TiO_2 doped with Ce probed with x-ray absorption spectroscopy, Applied Physics Letters, 2010, 97, 012104-012107

[27] H. Heinz, Clay minerals for nanocomposites and biotechnology: surface modification, dynamics and responses to stimuli, Clay Minerials, 2012, 47, 205-230

[28] P.J. Bardziński, On the impact of intermolecular interactions between the quaternary ammonium ions on interlayer spacing of quat-intercalated montmorillonite: A molecular mechanics and ab-initio study, Applied Clay Science, 2014, 95, 323-339

[29] W. Chen, P. Yuan, S. Zhang, Q. Sun, E. Liang, Y. Jia, Electronic properties of anatase TiO_2 doped by lanthanides: A DFT+U study, Physica B: Condensed Matter, 2012, 407, 1038–1043

[30] A.S. Brar, M. Mukherjee, S.K. Chatterjee, Microstructure and compositional assignments of acrylamide/vinylidene chloride copolymers using one and two dimensional nuclear magnetic resonance spectroscopy, European Polymer Journal, 2000, 36, 69–82

[31] A.G.A Lafi, Molecular dynamics in ion-irradiated poly(ether ether ketone) investigated by two-dimensional correlation dielectric relaxation spectroscopy, Polymers for Advanced Technologies, 2014, 25, 9–15

[32] H. Li, E. C. Minor, P.K. Zigah, Diagenetic changes in Lake Superior sediments as seen from FTIR and 2D correlation spectroscopy, Organic Geochemistry, 2013, 58, 125-136

[33] J.D. Begg, M. Zavarin, P. Zhao, S.J. Tumey, B. Powell, A.B. Kersting, Pu(V) and Pu(IV) sorption to Montmorillonite, Environmental Science and Technology, 2013, 47, 5146-5153

[34] M. Zavarin, B.A. Powell, M. Bourbin, P. Zhao, A. B. Kersting, Np(V) and Pu(V) ion exchange and surface-mediated reduction mechanisms on Montmorillonite, Environmental Science and Technology, 2012, 46, 2692-2698

[35] X. Liu, L. Wang, Z. Zheng, M.Kang, C. Li, C. Liu, Molecular dynamics simulation of the diffusion of uranium species in clay pores, Journal of Hazardous Materials, 2013, 244-245, 21-28

[36] L. Bian, Y. J. Shu, X. F. Wang, A molecular dynamics study on permeability of gases through parylene AF8 membranes, Polymers for Advanced Technologies, 2012, 11, 1520-1528

[37] S.N. Costa, F.A.M. Sales, V.N. Freire, F.F. Maia, E.W.S. Caetano, L.O. Ladeira, E.L. Albuquerque, U.L. Fulco, L-serine anhydrous crystals: structural, electronic, and optical properties by first-principles calculations, and optical absorption measurement, Crystal Growth and Design, 2013, 13, 2793-2802

[38] M. Segad, B. Jönsson, T. Åkesson, B. Cabane, Ca/Na Montmorillonite: Structure, Forces and Swelling Properties, Langmuir, 2010, 26, 5782-5790

[39] T.R. Zeitler, M.D. Allendorf, J.A. Greathouse, Grand Canonical Monte Carlo Simulation of Low-Pressure Methane Adsorption in Nanoporous Framework Materials for Sensing Applications, Journal of Physical Chemistry C, 2012, 116, 3492-3502

[40] E.R. Sylwester, E.A. Hudsona, P.G. Allen, The structure of uranium (VI) sorption complexes on silica, alumina, and montmorillonite, Geochimica et Cosmochimica Acta, 2000, 64, 2431-2438

[41] X. Tan, M. Fang, X. Wang, Sorption Speciation of Lanthanides/Actinides on Minerals by TRLFS, EXAFS and DFT Studies: A Review, Molecules, 2010, 15, 8431-8468

[42] S.K. Kim, H.D. Kwen, S.H. Choi, Radiation-induced synthesis of vinyl copolymer based nanocomposites filled with reactive organic montmorillonite clay, Radiation Physics and

Chemistry, 2012, 81, 519-523

[43] G. Geneste, J. M. Kiat, C. Malibert, First-principles calculations of quantum paraelectric $La_{1/2}Na_{1/2}TiO_3$ in the virtual-crystal approximation: Structural and dynamical properties, Physical Review B, 2008, 77, 052106-052109

[44] P. Joo, A. Fitch, S.H. Park, Transport in hydrophobized montmorillonite thin films, Environmental Science and Technology, 31, 1997, 2186-2192

[45] P. D. Dau, J. Su, H. T. Liu, J. B. Liu, D. L. Huang, J. Li, L. S. Wang, Observation and investigation of the uranyl tetrafluoride dianion ($UO_2F_4^{2-}$) and its solvation complexes with water and acetonitrile, Chemical Science, 2012, 3, 1137-1146

[46] T. Kozaki, T. Sawaguchi, A. Fujishima, S. Sato, Effect of exchangeable cations on apparent diffusion of Ca^{2+} ions in Na^- and Ca-montmorillonite mixtures, Physics and Chemistry of the Earth, 2010, 35 (6–8) 254-258

[47] B. Hammer, L.B. Hansen, J.K. Norskov, Improved adsorption energetics with in density-functional theory using revised Perdew-Burke-Ernzerhof functionals, Physical Review B, 1999, 59, 7413-7421

[48] T. Kawakami, Y. Tsujimoto, H. Kageyama, Xing-Qiu Chen, C. L. Fu, C. Tassel, A. Kitada, S. Suto, K. Hirama, Y. Sekiya, Y. Makino, T. Okada, T. Yagi, N. Hayashi, K. Yoshimura, S. Nasu, R. Podloucky, M. Takano, Spin transition in a four-coordinate iron oxide, Nature Chemistry, 2009, 1, 371-376

[49] J. Shi, H. Liu, Z. Lou, Y. Zhang, Y. Meng, Q. Zeng, M. Yang, Effect of interlayer counterions on the structures of dry montmorillonites with Si^{4+}/Al^{3+} substitution, Computational Materials Science, 69, 2013, 95-99

[50] D. Vanderbilt, Soft self-consistent pseudopotentials in a generalized eigenvalue formalism, Physical Review B, 1990, 41, 7892-7895

[51] J. P. Morel, V. Marry, P. Turq, N. M. Desrosiers, Effect of temperature on the retention of Cs^+ by Na-montmorillonite: microcalorimetric investigation, Journal of Materials Chemistry, 2007, 17, 2812-2817

[52] L.Bian, J.B.Xu, M.X. Song, H.L. Dong, F.Q.Dong, Effects of halogen substitutes on the electronic and magnetic properties of $BiFeO_3$, RSC Advances, 2013, 3, 25129–25135

[53] A. Halbritter, P. Makk, Sz. Mackowiak, Sz. Csonka, M. Wawrzyniak, J. Martinek, Regular Atomic Narrowing of Ni, Fe, and V Nanowires Resolved by Two-Dimensional Correlation Analysis, Physical Review Letters, 2010, 105: 266805-266809

[54] A. K. Nandy, P. Mahadevan, P. Sen, D. D. Sarma, KO_2: Realization of Orbital Ordering in a p-Orbital System, Physical Review Letters, 2010, 105, 056403-056407

[55] J. Simon, A. Felinger, Two-dimensional correlation analysis of the reproducibility of high-performance liquid chromatography columns, Journal of Chromatography A, 2015, 1384, 115–123

[56] S. Schinzel, M. Bindl, M. Visseaux, H. Chermette, Structural and Electronic Analysis of Lanthanide Complexes: Reactivity May Not Necessarily Be Independent of the Identity of the Lanthanide Atom-A DFT Study, Journal of Physical Chemistry A, 2006, 110, 11324-11331

[57] A. C. Lopes, M. P. Silva, R. Gonçalves, M. F. R. Pereira, G. Botelho, A. M. Fonseca, S. L. Mendez, I. C. Neves, Enhancement of the Dielectric Constant and Thermal Properties of α-Poly(vinylidene fluoride)/Zeolite Nanocomposites, Journal of Physical Chemistry C, 2010, 114, 14446-14452

[58] M.H. Bradbury, B. Baeyens, Sorption of Eu on Na- and Ca-montmorillonites: experimental investigations and modelling with cation exchange and surface complexation, Geochimica et Cosmochimica Acta, 2002, 66, 2325-2334

[59] A.C. Tsipis, C.E. Kefalidis, C.A. Tsipis, The role of the 5f orbitals in bonding, aromaticity, and reactivity of planar isocyclic and heterocyclic uranium clusters, Journal of the American Chemical Society, 130, 2008, 9144-9155

[60] I. C. Bourg, G. Sposito, A. C. M. Bourg, Tracer diffusion in compacted, water saturated bentonite, Clays and Clay Minerals, 2006, 54, 363-374

Tables

Table 1 Diffusion coefficients (D: $m^2 \cdot s^{-1}$) and activation energies (E: eV) of f-shell electrons/Ca-Mt.

Atom	Pure	5f-shell electron		4f-shell electron	
		D	E	D	E
Ca	7.8×10^{-9}	$3.7 \sim 4.4 \times 10^{-9}$ (A) $1.1 \sim 2.3 \times 10^{-9}$ (B)	39.95~40 (A); 0.64~2.25 (B)	$1.1 \sim 2.4 \times 10^{-9}$	0.88~1.1
O	1.7×10^{-11}	$10.3 \sim 11.5 \times 10^{-12}$ (A) $2.3 \sim 3.7 \times 10^{-12}$ (B)		$3.8 \sim 5.7 \times 10^{-12}$	
Si	8×10^{-12}	$11.1 \sim 12 \times 10^{-12}$ (A) $3 \sim 4.2 \times 10^{-12}$ (B)		$3.1 \sim 4.9 \times 10^{-12}$	
Al	7.6×10^{-12}	$10.5 \sim 11.7 \times 10^{-12}$ (A) $2.5 \sim 2.8 \times 10^{-12}$ (B)		$2.4 \sim 5.1 \times 10^{-12}$	

Table 2 Average bond lengths (Si-O and Al-O: nm), lattice lengths (a, b and c: nm) and lattice angles (α~β and γ: °) of Ca-Mt obtained from the experiment and various theoretical methods [7-15].

	exp	DFT-D2	vdW-TS	This work
Si-O	0.15~0.16	0.16~0.17	0.16~0.17	0.15~0.16
Al-O	0.16~0.17	0.17~0.18	0.19	0.16~0.17
a	0.51~0.52	0.51	0.52	0.48~0.5
b	0.88~0.9	0.9~0.91	0.89~0.91	0.83~0.87
c	1.2~1.6	1.35~1.47	1.41~1.5	1.39~1.45
α~β	89~91	89~90	89~90	90
γ	100~101	99~100	100	100~101

Table 3 The effective masses of holes and electrons at the [001] point. Unit: 10^{-31} kg.

	m_{hole}	$m_{electron}$
Pure Mt	2.86	51.3
5f-Mt	45.9~45.86 (A); 45.75~45.83 (B)	1316.47~968.72 (A); 599.5~403.01 (B)
4f-Mt	2.87~2.86	74.14~82.84

"A" reflects the $5f^n$-shell (n<7) electrons and the "B" indicates the $5f^n$-shell (n>7) electrons.

Table 4 Mulliken charges (e) of f-shell electrons/Ca-Mt.

Atom	Pure	5f-shell electron	4f-shell electron
Ca	0.47~0.49	0.14~0.2 (A); 0.4~0.46 (B)	0.4~0.46
O	-0.31~-0.24	-0.28~-0.15 (A); -0.31~-0.23 (B)	-0.3~-0.18
Si	0.51	0.51	0.51
Al	0.4~0.41	0.35~0.39 (A); 0.4~0.41 (B)	0.38~0.4

Captions

Figure 1 Free volumes (a) and adsorption energies (b) of f-shell electrons/Ca-Mt.

Figure 2 Structural properties of f-shell electron pillared Ca-Mt. The “L” denotes the bond length and “A” shows the bond angle.

Figure 3 The orbital fluctuation of f-shell electrons/Ca-Mt, which is observed via the 2D-CA technique. (a)-(d) reflect the model of Ca-Mt, the adsorption model of f-shell electrons/Ca-Mt, PDOSs of Ca-O, and illustration of orbital fluctuation by 2D-CA method.

Figure 4 Electronic structures and partial densities of states (PDOS) of Ca-Mt. The black lines show the PDOS of pure Ca-Mt; the red lines reflect the PDOSs of f-shell electrons/Ca-Mt.

Figure 5 Dielectric functions (a) and surface potentials (b) of Ca-Mt by the effect of 5f-shell and 4f-shell electrons.

Figure 6 Two-dimensional correlation patterns of the Ca electronic transitions induced by the 5f (a1-a2, a1’-a2’) and 4f (b1-b2, b1’-b2’) electrons. The data in a1-a1’ and b1-b1’ show the synchronous patterns, and a2-a2’ and b2-b2’ reflect the asynchronous patterns.

Figure 7 Two-dimensional correlation patterns of the O electronic transitions by the effect of 5f (a1-a2) and 4f (b1-b2) electrons.

Figure 8 Two-dimensional correlation patterns of the Si and Al electronic transitions by the effect of 5f (a1-a2, a1'-a2') and 4f (b1-b2, b1'-b2') electrons.

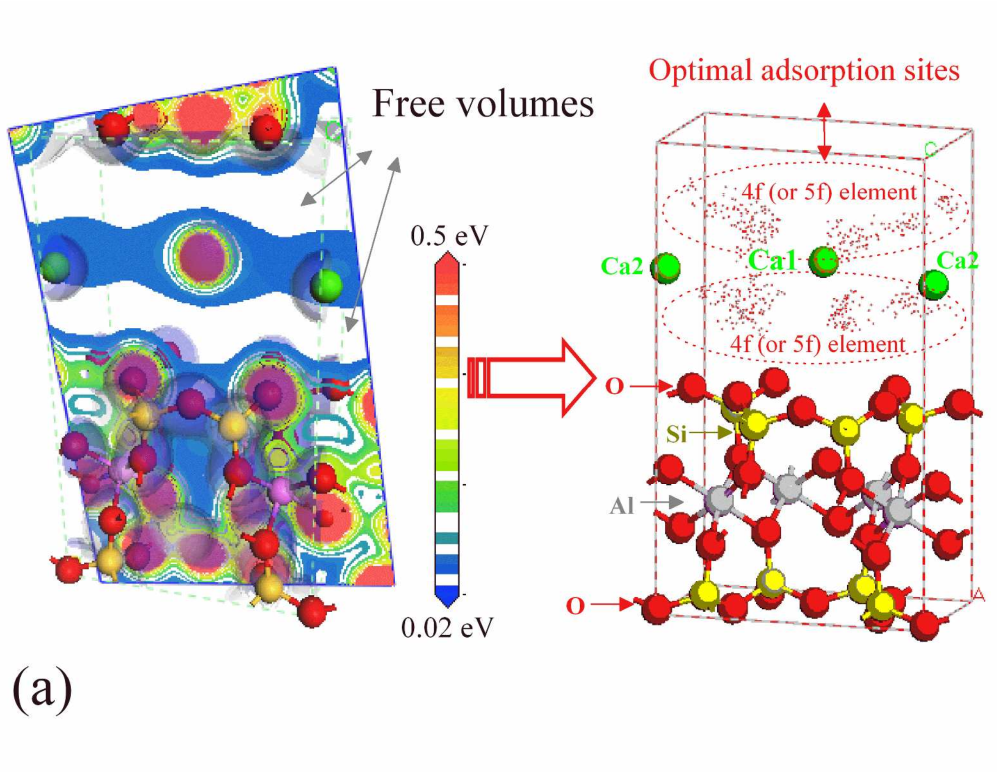

279x215mm (300 x 300 DPI)

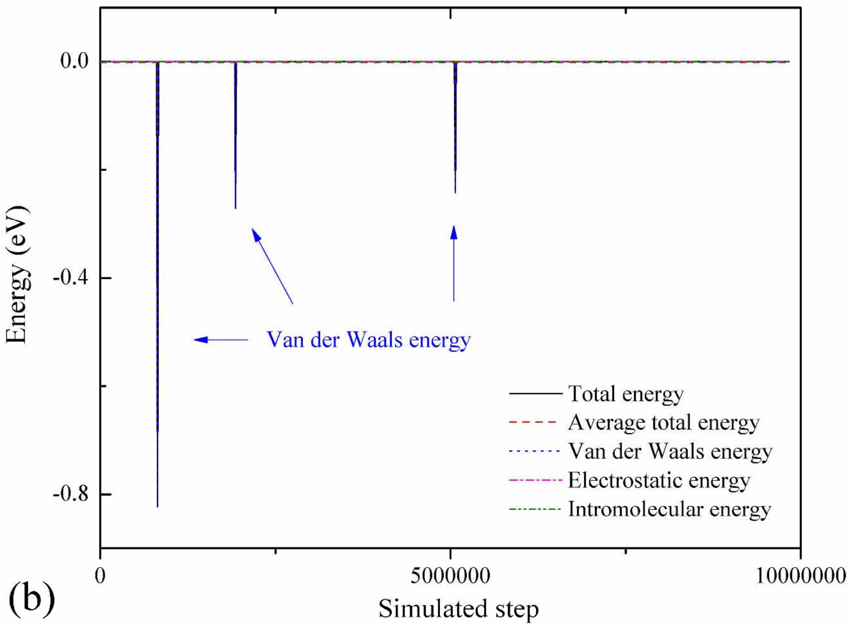

279x215mm (300 x 300 DPI)

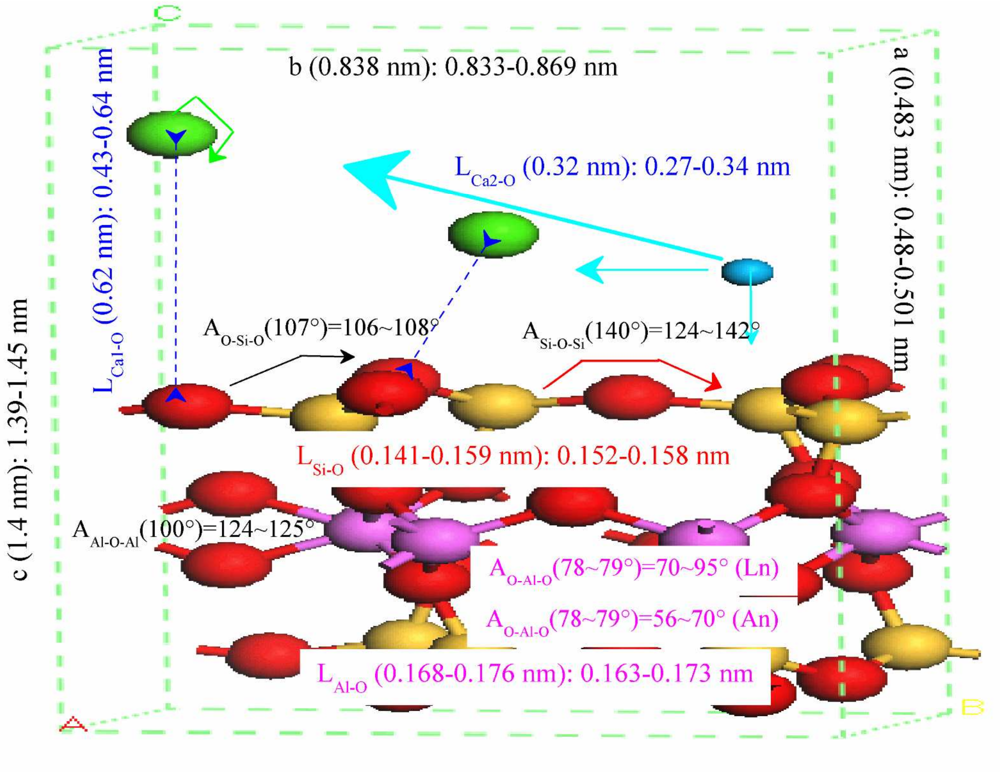

279x215mm (300 x 300 DPI)

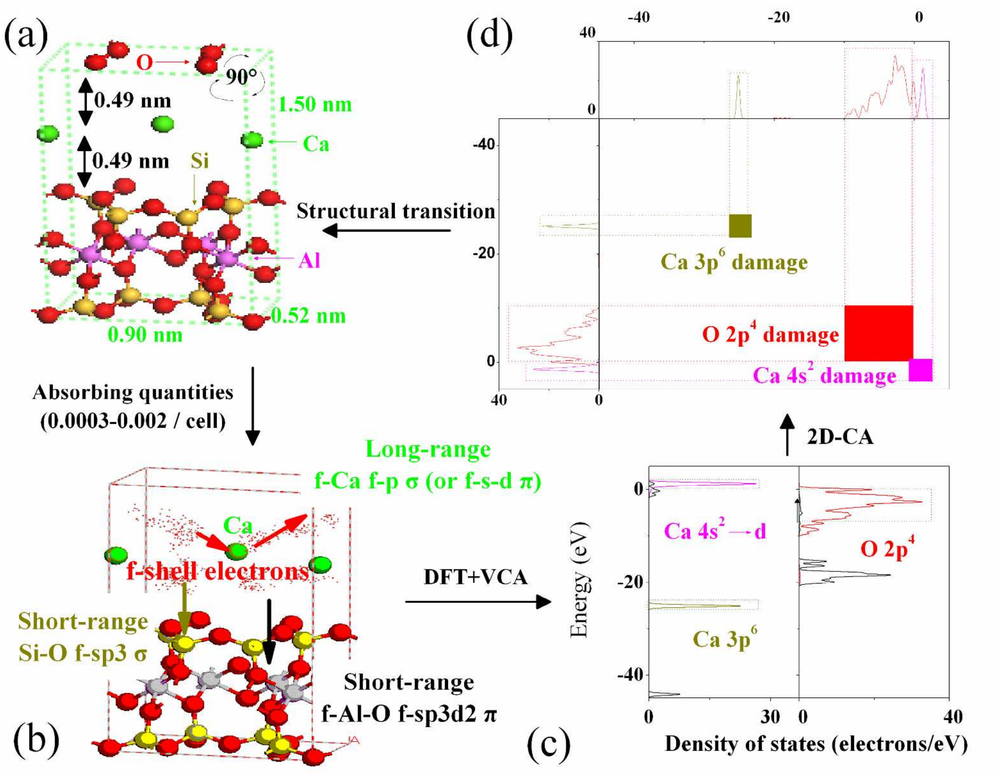

279x215mm (300 x 300 DPI)

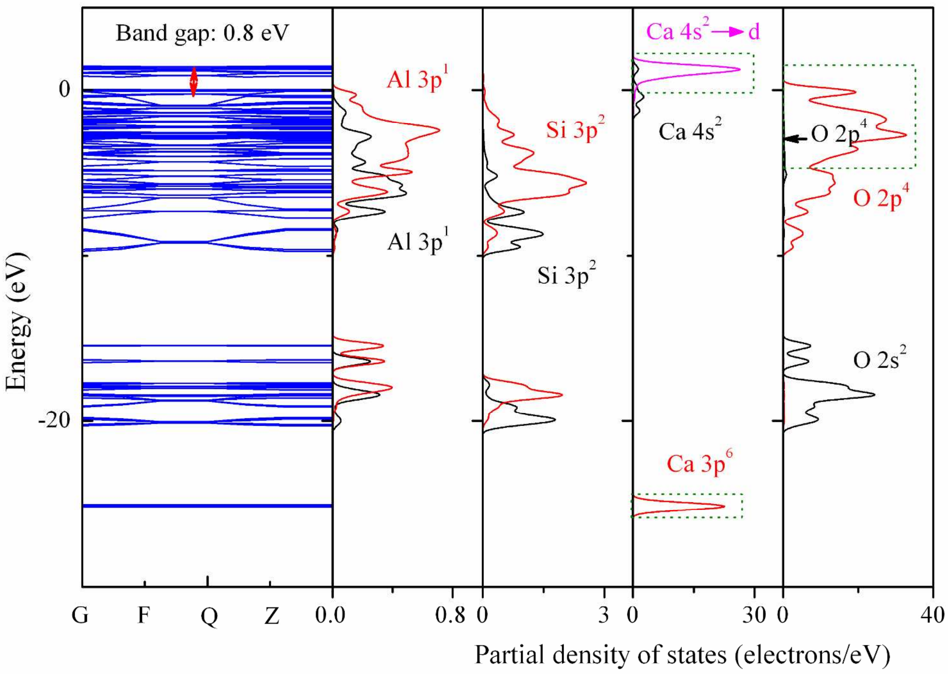

279x215mm (300 x 300 DPI)

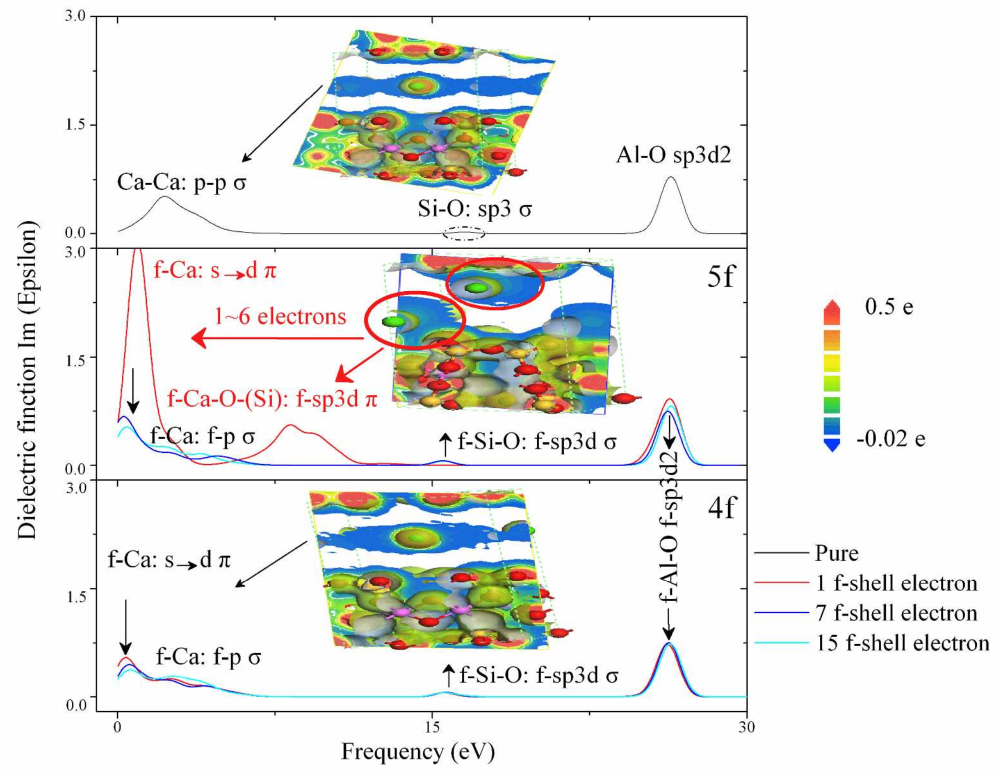

279x215mm (300 x 300 DPI)

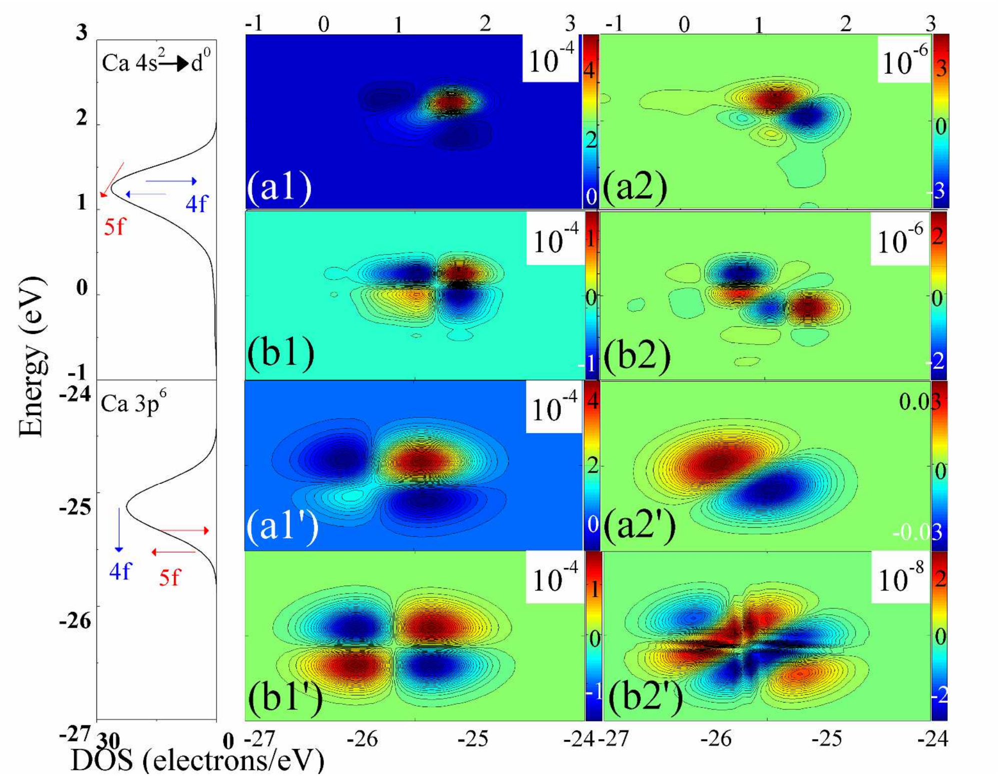

279x215mm (300 x 300 DPI)

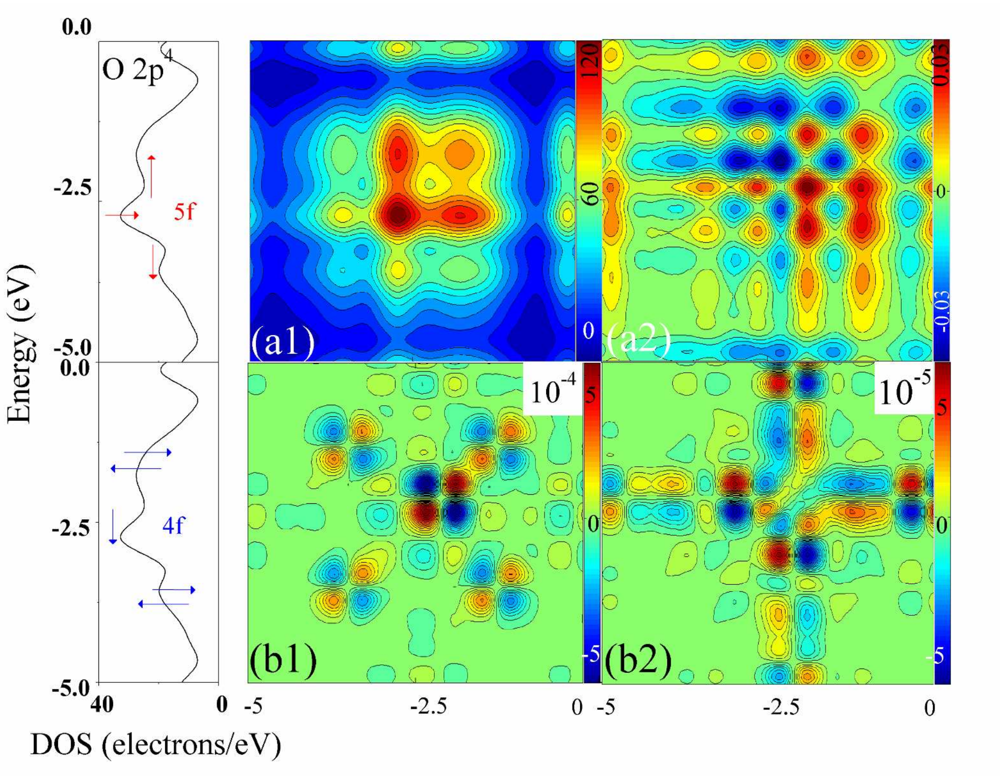

279x215mm (300 x 300 DPI)

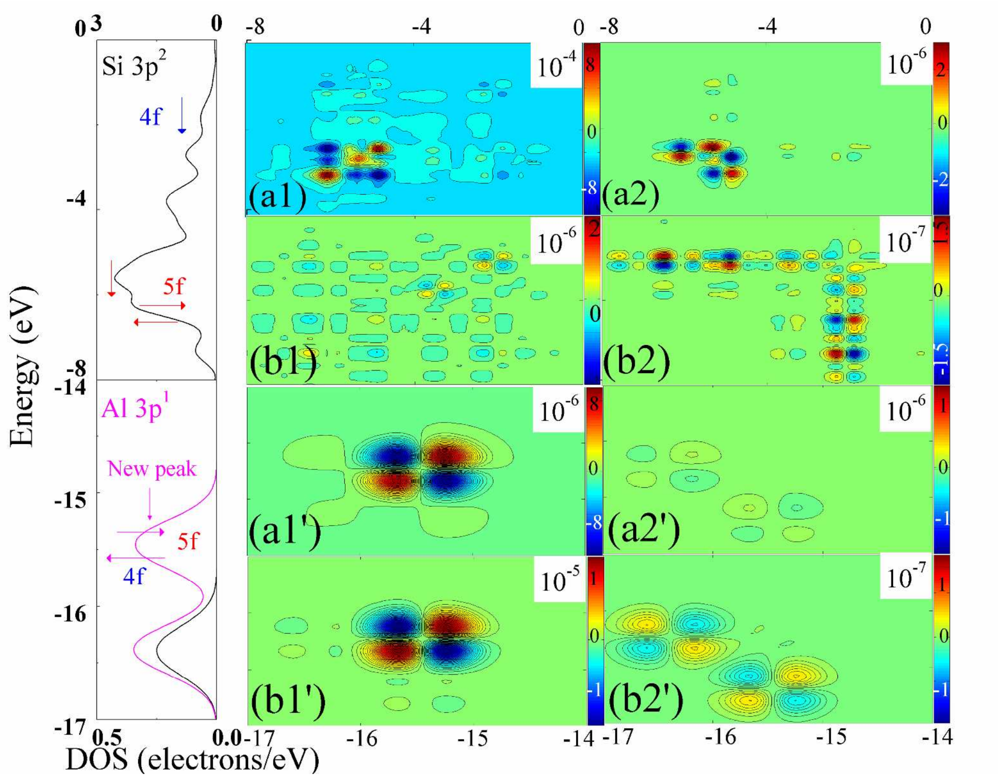

279x215mm (300 x 300 DPI)